NJC

PAPER

View Article Online
View Journal | View Issue

Published on 24 June 2019. Downloaded by National Sun Yat Sen University on 3/23/2020 10:57:07 AM.

Check for updates

Cite this: *New J. Chem.*, 2019, 43, 12241

PCL–DOX microdroplets: an evaluation of the enhanced intracellular delivery of doxorubicin in metastatic cancer cells *via in silico* and *in vitro* approaches†

Aman Chandra Kaushik,‡[ah] Ajay Kumar,‡[bc] Chun-Yen Yu,‡[d] Shiao-Wei Kuo,[e] Shih-Shin Liang,[f] Satya P. Singh,[g] Xiangeng Wang,[a] Yan-Jing Wang,[a] Chung-Kun Yen,[c] Xiaofeng Dai,*[h] Dong-Qing Wei,*[a] Cheng-Tang Pan*[ci] and Yow-Ling Shiue*[b]

Researchers have promoted the use of polymer microspheres in medical engineering and biotechnology, such as embedded drug delivery with polylactic acid microspheres. Polycaprolactone (PCL) is a kind of semi-crystalline polymer, which can be utilized in many varieties of organic solvent. Therefore, PCL has been used as a controlled-release drug carrier for long-term treatment. This study focuses on the fabrication process of biodegradable PCL microcarriers with uniform and controllable particle size (size range is ~5–100 μm) *via* an emulsion-solvent evaporation process with ultrasonic micro-droplet atomization technology. Through ultrasonic atomization, micro-droplets of PCL solution were sprayed out directly with highly uniform particle size. The oil micro-droplets of PCL were collected with an aqueous stream in an emulsion process to form a water–oil–water emulsion. The ultrasonic atomizer assisting the emulsification process was adjusted *via* the stirring equipment to enhance the particle size uniformity. As a result, PCL micro-droplets were sprayed into aqueous solution due to the vertical flow field made by the stirring equipment. The yield rates of PCL microcarriers were improved effectively. Moreover, the cancer pharmaceutical doxorubicin (DOX) was added into the process to obtain drug-loaded microcarriers. The drug-loading efficiency in this process was ~42.2%, and the encapsulation efficiency of the microcarriers was ~3.21%. Further, we performed docking and MD simulations of the polycaprolactone–doxorubicin hydrochloride interaction that showed their binding affinity and later validated potential inhibitors. Additionally, we have successfully established the dynamic behavior of an entire biochemical pathway in the presence of polycaprolactone with doxorubicin hydrochloride, using a systems biology approach.

Received 13th April 2019,
Accepted 23rd June 2019

DOI: 10.1039/c9nj01902b

rsc.li/njc

1. Introduction

Hepatocellular carcinoma (HCC) is one of the top 10 causes of death in Taiwan, and remains a major public health issue. Common treatments for HCC include (1) surgical resection,[1,2] (2) local alcohol injection,[3,4] and (3) chemotherapy.[5,6] Surgical resection is the optimal treatment,[7,8] however it affects the hepatic function of the residual liver and therefore is not suitable for every patient. For huge and unresectable tumors, transarterial chemoembolization (TACE) has been used as a

[a] *The State Key Laboratory of Microbial Metabolism, School of Life Sciences and Biotechnology, Shanghai Jio Tong University, Shanghai, 200240, China. E-mail: amanbioinfo@sjtu.edu.cn, wangxiangeng@sjtu.edu.cn, tangtangfeiwu@qq.com, dqwei@sjtu.edu.cn*
[b] *Institute of Biomedical Sciences, National Sun Yat-Sen University, Kaohsiung City, 804, Taiwan. E-mail: ajaynsysu@mem.nsysu.edu.tw, shirley@imst.nsysu.edu.tw*
[c] *Department of Mechanical and Electro-Mechanical Engineering, National Sun Yat-sen University, Kaohsiung City 804, Taiwan. E-mail: alden0113@gmail.com, pan@mem.nsysu.edu.tw*
[d] *From the Liver Transplantation Program and Departments of Diagnostic Radiology, Kaohsiung Chang Gung Memorial Hospital and Chang Gung University College of Medicine, Kaohsiung, Taiwan. E-mail: y7192215@ms17.hinet.net*
[e] *Department of Materials and Optoelectronic Science, National Sun Yat-Sen University, Kaohsiung 80424, Taiwan. E-mail: kuosw@faculty.nsysu.edu.tw*
[f] *Department of Biotechnology, College of Life Science, Kaohsiung Medical University, Kaohsiung, Taiwan. E-mail: liang0615@kmu.edu.tw*
[g] *School of Electrical and Electronic Engineering, Nanyang Technological University, Singapore. E-mail: satya002u@gmail.com*
[h] *Wuxi School of Medicine, Jiangnan University, Wuxi, China. E-mail: xiaofeng.dai@jiangnan.edu.cn*
[i] *Institute of Medical Science and Technology, National Sun Yat-Sen University, Kaohsiung City 804, Taiwan*

† Electronic supplementary information (ESI) available. See DOI: 10.1039/c9nj01902b

‡ These authors contributed equally.

Published on 24 June 2019. Downloaded by National Sun Yat Sen University on 3/23/2020 10:57:07 AM.

standard cancer treatment with drug-loaded microspheres in recent years.[1,9–11]

The occurrence of HCC can be divided into two types: primary hepatic cancer and liver metastasis.[2,12] People demonstrating primary hepatic cancer symptoms are evaluated for hepatitis, cirrhosis, and then HCC, which is caused by hepatitis B, hepatitis C, heavy alcohol use, obesity, *etc.*[13,14] Cancer that has spread from elsewhere to the liver, known as liver metastasis, is more common than that which starts in the liver.[15,16] Liver blood and nutrients are supplied by the hepatic artery and hepatic portal vein in ratios of 25% and 75%, respectively.[17–19] Conversely, during HCC blood and nutrients are obtained mostly from the hepatic artery. Therefore, TACE utilizes HepaSphere with the cancer drug DOX to achieve embolization of the hepatic artery and release of the cytotoxic drug simultaneously, which will make an unresectable tumor shrink by a considerable amount due to a shortage of nutrients and the drug treatment.[20–22] Then, surgical resection can take over. Interestingly, these kinds of microsphere provide an innovative way of drug-delivery, which allows drug administration in the needed amount at the right time.[23–25] They also protect drugs until they reach the target tissue or organ, minimizing side effects and considering patient comfort through using infrequent injection as the route of administration (once per month or less). Since different sizes of vessels around the tumor need to be embolized, these microspheres require the control of particle size distribution (PSD) and encapsulation efficiency (EE). With proper microsphere PSD, the efficacy of embolization treatment can be greatly improved.[26–29]

Polycaprolactone (PCL) is biodegraded by outdoor living organisms (bacteria and fungi), but there is a lack of suitable enzymes in animals and the human body that can degrade PCL rapidly.[30–33] This does not indicate that it is not resorbable in human bodies, but rather, it takes much longer, propagating first *via* hydrolytic degradation or enzyme-catalyzed hydrolysis.[34–37] After hydrolysis, it can be degraded into ε-hydroxy caproic acid, which is then metabolized by cells (phagosomes of macrophages and giant cells). In general, the complete degradation of PCL takes 1–3 years in biological media, which is slower than other polymers, so PCL is most suitable for use in long-term drug delivery systems.[38–41]

Compared with drug-eluting beads, drug-loaded polymer microspheres encapsulate drugs during the fabrication process rather than absorbing drugs after fabrication.[42–45] For classification, drug-loaded polymer microspheres are a type of medicine and HepaSphere is a type of medicinal material. The PSD and EE of HepaSphere can be controlled during absorption. PSD and EE are important indicators for polymer microspheres during fabrication.[46,47] For wide applications, a fabrication method producing microspheres with controllable PSD and high EE for mass production at low cost could be a great potential technology; this is also a focus of this study.

Systems biology is an interdisciplinary field of study that focuses on using mathematical and computational modeling to gain insights into complex biological organizations.[48,49] Rather than using traditional reductionism, systems biology employs a holistic approach to explore complex interactions and relationships in biological systems. Part of the aim of this field is to investigate and model how the emergent and existing properties of organisms, tissues, cells, and genes function together as a system.

There are various approaches for studying biological processes using molecular interaction networks.[50] This has resulted in the emergence of functionally related sub-networks known as "functional modules".[51,52] The modular organization of function has been shown to exist across species, and can be used to predict gene functions. Similar networks have also been generated using co-expression data, genetic interaction data, and combinations of data types.[53] However, a disadvantage is that these networks contain false positive and false negative interactions, which may distort our understanding of functional organizations.[53,54]

1.1. Polymer microsphere manufacture *via* emulsion-solvent evaporation (ESE)

Several methods relating to microsphere fabrication have been described in the literature, including phase separation, spray drying, and solvent evaporation techniques.[55] Of these, spray drying is uncomplicated in operation. However, its dryness and high temperature aren't suitable for some polymers or drugs, and microspheres obtained using it have poorly controlled PSDs due to the high-energy process.[56] Phase separation utilizes lots of organic solvents as aggregating agents to prepare microspheres. These solvents can have toxicity and lead to environmental pollution and residue problems when used for microspheres.[57] Compared to these techniques, microencapsulation *via* ESE has been widely applied in pharmaceutical industries to obtain uniform microspheres without high temperatures or toxic solvents. Microsphere formation is accompanied by solvent evaporation, transforming disperse phase droplets into solid particles, and any residual solvent in the microspheres is eliminated through the cleaning and drying process. ESE contains three important basic steps: (1) emulsion droplet formation;[58] (2) solvent removal;[59] and (3) drug loading.[59,60]

The formation of emulsion droplets determines the PSD of microspheres.[61,62] The stability of the emulsion droplets and the fabrication environment can influence the shape and morphology of microspheres. Therefore, it is necessary to study the impact of emulsion droplet formation and the stability of these factors.

In this research, we present a pathway network representing a global biological function. Through incorporating pathways from multiple data sources, we aim to maximize functional coverage while minimizing the overlap between pathways. To assess the ability of our network to interpret disease functions, we mapped a broad range of disorders onto the network, before focusing more specifically on cancer. Disease pathway "modules", or clusters, are known to form within molecular networks, showing overlap with functional modules.[63] Cancer genes especially have been found to be highly connected, with different types of cancer forming highly connected overlapping modules. Our representation provides a higher-level view of the pathways and functions affected by diseases, without the inaccuracies that are generally inherent in molecular-level interaction data.

The wet-lab study reports the capabilities of two techniques, individually and in combination, to generate uniform biodegradable

Published on 24 June 2019. Downloaded by National Sun Yat Sen University on 3/23/2020 10:57:07 AM.

microcarriers with precisely controllable size, from 5–100 μm in diameter. Furthermore, this technology demonstrated drug-loaded microcarrier fabrication with doxorubicin. Doxorubicin is a common cancer drug, which can treat breast cancer, leukemia, lung cancer, liver cancer, *etc.*

2. Methodology

PCL (M_w = 10 000) was obtained from Sigma-Aldrich. Polyvinyl alcohol (PVA, 88% hydrolyzed) was obtained from Sigma-Aldrich. Ethyl acetate (EA) was obtained from Twangy, Taiwan. Different hydrophile lipophilic balance (HLB) surfactants were used: sodium lauryl sulfate (SDS, 95%, M_w: 288, HLB = 40), obtained from Scharlau; and Tween 20 (HLB = 16.7), Tween 80 (HLB = 15), and Span 80 (HLB = 4.3), obtained from First Chemical Works, Taiwan. PBS (pH = 7.4) was obtained from Fluka. DOX was obtained from Concord Biotech Limited. Fetal bovine serum (FBS) and PS were obtained from Sigma-Aldrich.

2.1. Drug-loaded PCL microsphere fabrication with DOX *via* EUA (emulsification assisted with ultrasonic atomization)

Polymer microspheres are medical materials, which can be considered as microcarriers to carry different kinds of drugs for drug-delivery systems in the human body.[64,65] Through EUA technology, DOX was encapsulated into PCL microspheres *via* the multiple emulsion type W1/O/W2. This study further proposed a syringe with built-in stirring components to solve the uneven W1/O emulsion, as shown in the ESI† (Fig. S1). A stirring component equipped inside the syringe can keep the W1/O emulsion under stable mixing.

Through this innovative syringe, the W1/O emulsion was supplied to the ultrasonic atomizer (ESI,† Fig. S2) (amplitude: ~8–10 μm) at 0.3 mL min^{-1}, and this was sprayed into 300 mL of PVA solution (with 0.5 wt% SDS) under 200 rpm stirring to form the multiple emulsion type W1/O/W2. The W1/O/W2 emulsion solution underwent 30 min of pre-emulsification, then was poured into 700 mL of DI water under 100 rpm stirring for 1 hour of emulsification.

The particle size of the DOX original powder was ~5–20 μm, as shown in the ESI† (Fig. S1), which was too big to be encapsulated in DLPMs, whose particle size was supposed to be ~5–100 μm. Therefore, micronizing the DOX powder was essential. During the micronization, alcohol was chosen as a solvent to dissolve the DOX powder; they were mixed together under ultrasonic vibration *via* an ultrasonic cleaner.

2.2. Molecular docking

The polycaprolactone (CID 10401) and doxorubicin hydrochloride (CID443939) three-dimensional structures were downloaded from PubChem.[66]

2.3. Molecular dynamics (MD) simulations

Polycaprolactone and doxorubicin hydrochloride docked complexes were subjected to molecular dynamics simulations using Desmond v4.[67,68]

2.4. Systems biology approach

Pharmacokinetics is a branch of pharmacology that focuses on the efficacy of drugs administered to a living organism.[69] This study encompasses the time course of drug metabolism, absorption, distribution, bioavailability, and excretion. In contrast to pharmacodynamics (PD), which is dedicated to the effects of drugs on organisms, pharmacokinetics is concerned with eliminating toxicity as well as improving the effectiveness of drugs given to patients.

2.5. Time course and stochastic simulations

Mass action kinetics are used in the chemical engineering and chemistry fields to demonstrate direct relationships between the rate of reaction and the product of reactant concentrations.[70] With mass action kinetics, researchers can accurately predict whether a chemical reaction is second-order, first-order, zero-order, or a reversible reaction. The ordinary differential equation used for mass-action kinetics produces polynomial vector fields.[71] For example;

$$\begin{aligned} &\mathrm{A} + \mathrm{B} \rightarrow \mathrm{C} \\ &[\text{rate of reaction}] = k[\mathrm{A}][\mathrm{B}] \end{aligned} \tag{1}$$

where [B] and [A] represent the concentrations of B and A, respectively and k denotes the rate constant or proportionality rate. This value is always greater than zero, and is influenced by the temperatures of the reactants, X. Hence, the rate of a chemical reaction can be written as follows:

$$\frac{\mathrm{d}[\mathrm{A}]}{\mathrm{d}t} = -k[\mathrm{A}][\mathrm{B}] \tag{2}$$

$$\frac{\mathrm{d}[\mathrm{B}]}{\mathrm{d}t} = -k[\mathrm{A}][\mathrm{B}] \tag{3}$$

$$\frac{\mathrm{d}[\mathrm{C}]}{\mathrm{d}t} = k[\mathrm{A}][\mathrm{B}] \tag{4}$$

2.6. Zeta potential

Zeta-potential measurements were performed to study the colloidal stability of the prepared small particles.[72] These calculate the difference between the dispersed field and particles. The zeta potential is an electrical potential that is present at the double layer boundary of a particle when the particle moves.[73] In this research a sample of solution A was immersed in 2 mL of PBS solution under constant stirring for 30 min at room temperature. Solution B was prepared with solution A. Solution A was diluted with 2 mL of deionized water under constant stirring for 30 min at room temperature.

2.7. The *in vitro* release-rate profile of DLPMs

The *in vitro* release by the DLPMs was measured in three solutions: PBS (pH = 7.4); PS dissolved in PBS (0.005 g mL^{-1}); and FBS dissolved in PBS (150 μL mL^{-1}) at 37 °C for one month. In a 1.5 mL centrifuge tube, approximately 10 mg of DLPMs was suspended in 1 mL of solution, as shown in Fig. 1. DLPMs with sizes of 20–100 μm and 100–200 μm were tested in the three

Published on 24 June 2019. Downloaded by National Sun Yat Sen University on 3/23/2020 10:57:07 AM.

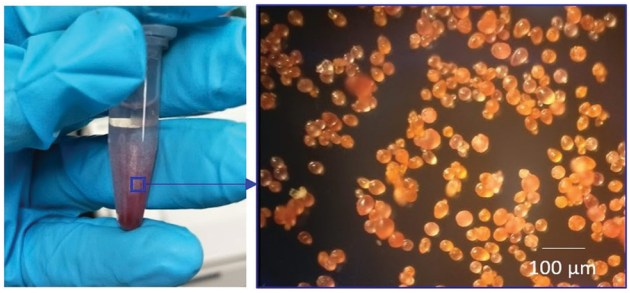

Fig. 1 Samples examined in release experiments used PBS solution, PS/PBS solution, or FBS/PBS solution.

Table 1 Samples used in the release experiments

PSD (10 mg of DLPMs)	PBS (pH = 7.4)	Lipase PS (0.005 g mL^{-1})	FBS (15%)
20–100 μm	1000 μL	—	—
20–100 μm	1000 μL	0.005 g	—
20–100 μm	850 μL	—	150 μL
100–200 μm	1000 μL	—	—
100–200 μm	1000 μL	0.005 g	—
100–200 μm	850 μL	—	150 μL

solutions, and Table 1 shows all sample configurations. The released solution was collected *via* centrifugation periodically (3 or 4 days) and it was replaced with the same amount of fresh solution. The amount of released DOX was directly analyzed using a spectrophotometer at a wavelength of 230 nm. Empty PCL microspheres with the three solutions were used as blanks. Release profiles were calculated in terms of cumulative release (%) with incubation time. Each sample was assayed in triplicate. The surface morphologies of the DLPMs before and after the release study were examined *via* SEM.

2.8. Cancer cell lines derived from leukemia (CCRF-CEM) and HCC (Huh-7)

Two cancer cell lines were used to evaluate the apoptotic effects of the DLPMs. Cells were maintained in a humidified incubator with 5% CO_2 at 37 °C with Dulbecco's Modified Eagle's Medium (Thermo Fisher Scientific) containing 15% (v/v) fetal bovine serum (Biological Industries), 50 IU mL^{-1} penicillin, 50 μg mL^{-1} streptomycin (MediaTech), and 1% nonessential amino acids. Cells (1×10^5) were seeded in a 24-well plate overnight and treated with smaller DLPM spheres of 20–100 μm (L: 0.22%; H: 0.97%) and larger DLPM spheres of 100–200 μm (L: 0.29; H: 0.60%) at 1 mg mL^{-1} in a Corning® Transwell® polyester membrane cell culture insert (#CLS3470-48EA) with a pore size of 0.4 μm to precisely separate cells from the DLPMs. However, the culture medium containing gradually releasing DOX could freely circulate between the upper and lower chambers. After 48 h, cells were collected and subjected to an apoptosis assay *via* the quantification of phosphatidylserine exposure. Briefly, cells were centrifuged for 5 min at 700 × *g* and resuspended in Annexin V Binding Buffer (#BMS306F1, Bender MedSystems, Vienna, Austria). Annexin V analysis with FITC-labeled nucleotides (R & D Systems, Minneapolis, Canada), as well as propidium iodide staining, was carried out following the manufacturer instructions. Following incubation for 10 min, the samples were subjected to flow cytometric analysis (NovoCyte™ 2000, ACEA, San Diego, CA, USA) and analysis using NovoExpression™ software (ACEA, San Diego, CA, USA), with excitation and emission wavelengths of 488 and 530 nm, respectively. One-way analysis of variance was used to evaluate the significance of apoptotic effects among different groups, followed by a Scheffe multiple comparison test. A P-value < 0.05 is considered to be of statistical significance.

3. Results and discussion

3.1. Drug-loaded microspheres

3.1.1 DLPMs (DOX-loaded PCL microspheres) made *via* EUA (emulsification assisted with ultrasonic atomization). W1/O/W2 (water–oil–water) (W1: Dox; O: PCL; W2: PVA): As the W1/O emulsion droplets contacted the PVA solution, lipophilic PVA covered them, while solvent EA and DOX solution diffused into the PVA solution (ESI,† Fig. S1). To avoid the continuous leakage of DOX solution out of the microspheres, solvent EA needs to be extracted rapidly to form a shell around the W1/O emulsion droplets.

Therefore, DLPMs were fabricated, dried naturally and stored in a tube to avoid degradation *via* hydrolysis in moist environments or bacterial growth. Dry DLPMs demonstrated some drug crystallization on the surface, as shown in the ESI† (Fig. S2). Since the DOX solution encapsulated by the PCL microspheres dried up, DOX crystallization arose and the DLPMs formed matrix structures. The DOX spectrum corresponds with ultraviolet (UV) light of 100–400 nm, therefore DLPMs have a fluorescence reaction under UV light, which can be used to check whether DOX was encapsulated in the microspheres or not, as shown in the ESI† (Fig. S3).

The DOX spectrum was first analyzed *via* a UV spectrophotometer (Jasco, Model V-770) as shown in Fig. 2(A). There was a strong absorbance at a wavelength of 230 nm. Accordingly, 230 nm was used to generate a calibration curve using another spectrophotometer (Nanodrop 2000, Thermo Fisher Scientific). To establish a calibration curve, DOX (0.015–0.4 mM) was dissolved in DI water and 1 μL of this solution was measured at 230 nm. The calibration curve is shown in Fig. 2(B); it is a linear curve and, from this, unknown concentrations of DOX solution from DLE and EE experiments can be calculated (Fig. 3).

3.2. EE (encapsulation efficiency) and DLE (drug-loading efficiency)

The DLE of DLPM *via* this formulation (W1/O/W2) was calculated to be 38.2–42.2%. The EEs of DLPMs with sizes of 5–30 μm, 30–50 μm, 50–100 μm, 100–200 μm, and 200–500 μm were found to be 3.21%, 1.54%, 0.97%, 0.97%, and 0.5%, respectively, as shown in the ESI† (Table S1). It was observed that smaller DLPMs had higher EEs. In this process, microdroplets (W1/O) from atomization were assumed to perfectly consist of homogeneous PCL solution and DOX solution. With the rapid extraction of EA during atomization, the proportion of DOX solution in the microdroplets (W1/O) increased.

 This journal is © The Royal Society of Chemistry and the Centre National de la Recherche Scientifique 2019

Published on 24 June 2019. Downloaded by National Sun Yat Sen University on 3/23/2020 10:57:07 AM.

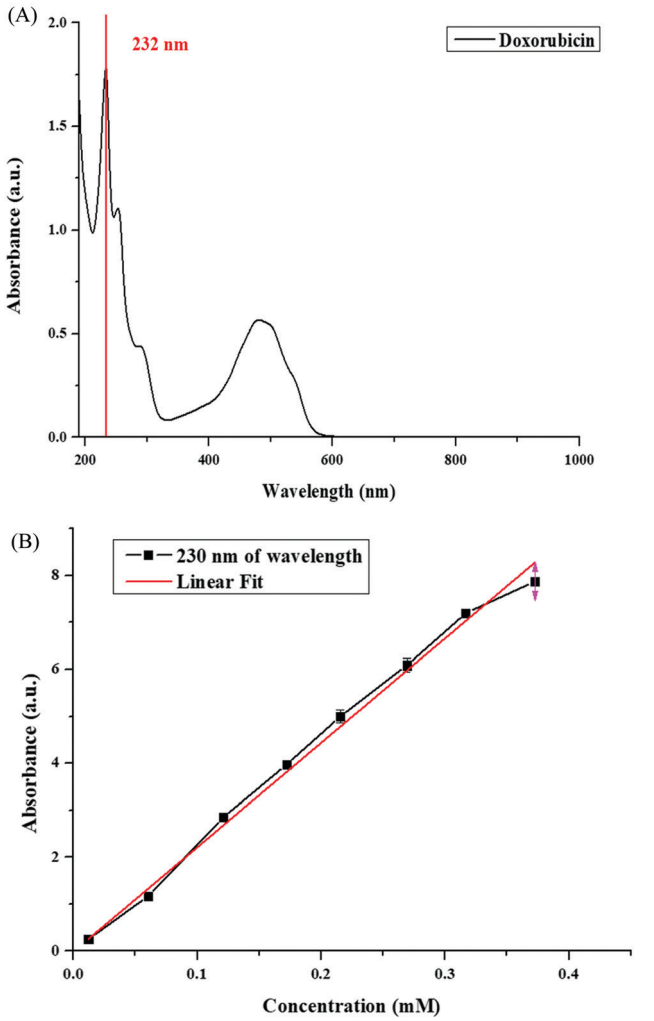

Fig. 2 (A) The DOX spectrum, with strong absorbance at a wavelength of 230 nm. (B) The calibration curve of DOX solution (0.015 to 0.4 mM).

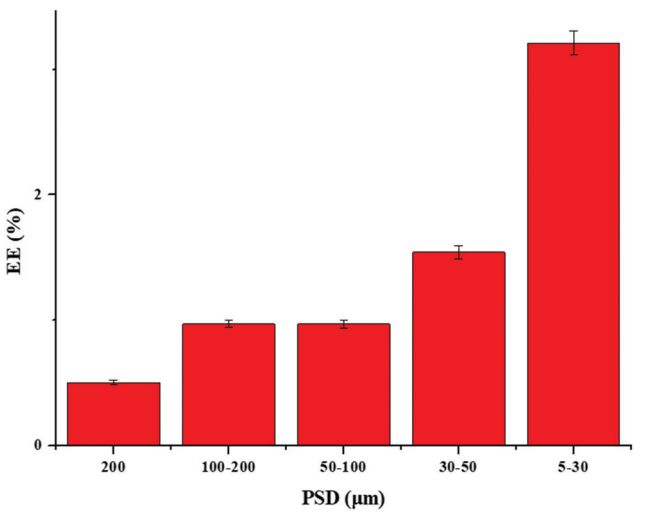

Fig. 3 A histogram representing the EE of DLPMs with different particle size distributions.

Smaller microdroplets with a larger surface area underwent EA evaporation faster than bigger ones. Therefore, the proportions of DOX solution and EA in the microdroplets changed during flight, and the smaller microdroplets had a higher DOX solution ratio. Then, the mixture was submerged into PVA solution and EA was extracted again, leading the polymer to precipitate on the surface of the microdroplets, avoiding the leakage of drug solution out of the microdroplets. Due to the smaller microdroplets having a higher DOX solution ratio, a formation process involving smaller DLPMs encapsulated more DOX solution and obtained higher EE values.

However, DOX solution was made of DOX powder dissolved in DI water at a 1 : 20 ratio by weight (0.15 g of DOX in 3 g of DI water). For this reason, the EE of the DLPMs was 3.21% at 5–30 μm, which indicates that 10 mg of 5–30 μm DLPMs encapsulated 0.321 mg of DOX and 6.42 mg of DI water (suggesting an EE of DOX solution ≈ 64.2%). Therefore, at a weight ratio of 1 : 20 of DOX solution, there were certain limits on the EE using the W1/O/W2 system.

The other reason for the low EE is because it was a challenge for hydrophobic PCL to encapsulate hydrophilic DOX. In this situation, the solution concentration (viscosity affects the fluidity of DOX solution out of the microspheres) and pre-emulsion time (with a longer pre-emulsion time, the chances of DOX solution diffusing out of the microspheres increases) influence the EE. Moreover, DOX crystals arose upon the surface of the DLPMs, so each cleaning process can remove these and reduce the EE of the DLPMs.

3.3. Colloidal stability analysis

The zeta potential is the average electro-kinetic potential of a colloidal system, or it is the real surface charge of a polydisperse system. A high magnitude of zeta potential suggests a high stability dispersion.[72,74] High stability polymeric materials are important for use in bio-medical applications.[75,76] A potential of more than ±30 mV in magnitude is referred to as a stable system. The zeta potential of a PCL sample observed in phosphate buffer (PBS) was found to be −885 mV, which may be due to masking effects from the surface charge of the PBS used as a solvent during the measurements. Therefore, to assess the real surface charge of a PCL sample, the above dispersing medium was diluted with deionized water. The zeta potential observed for the PCL dispersion was found to be −89.25 mV, suggesting a stable polymeric system. The pH is also a vital factor for ensuring stability and it has been reported that dispersions are more stable near pH 7[73]. The pH of the PBS–water–PCL system was measured to be 7.4, signifying the stability of the polydisperse system.

3.4. *In vitro* release rate profile of the DLPMs

In vitro DOX release from the DLPMs was carried out in 1 mL of PBS (pH = 7.4) solution, PBS solution containing PS (0.005 g mL^{-1}), and PBS solution containing FBS (150 μL mL^{-1}) at 37 °C for one month. As seen in Fig. 4, burst release related to DOX entrapped near the surface of the DLPMs occurred during the first week, and this was followed by sustained release over the second week.

Published on 24 June 2019. Downloaded by National Sun Yat Sen University on 3/23/2020 10:57:07 AM.

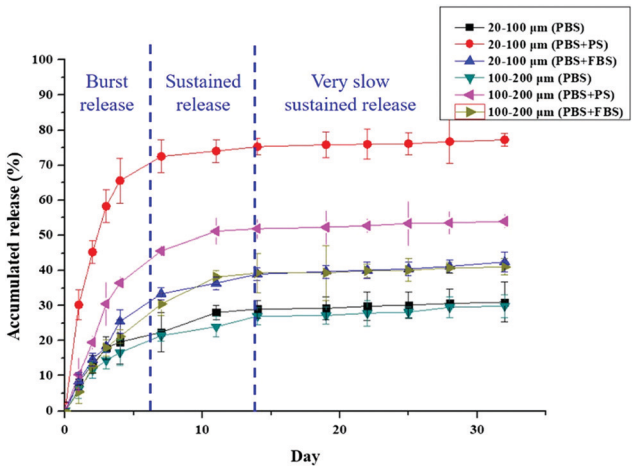

Fig. 4 Release experiments were carried out in PBS (pH = 7.4), PBS containing PS (0.005 g mL^{-1}), and PBS containing FBS (150 μL mL^{-1}) at 37 °C for one month.

After about two weeks, DOX was released very slowly. The results also indicated that the DLPMs with a size of 5–20 μm had faster release efficacy than the DLPMs with a size of 100–200 μm due to the larger surface area. About 70% and 50% of DOX was released, respectively, from 5–20 μm and 100–200 μm DLPMs in PBS solution containing PS in the initial two weeks. In this case, because PCL can degrade rapidly and completely in PBS containing PS through cleavage of the ester bonds of PCL, the rate of drug release increased apparently and the color of the DLPMs can be observed to be lightened obviously compared with the other samples, as shown in Fig. 5.

SEM images of the DLPMs are shown in Fig. 6A–D. The DLPMs possessed a spherical shape with a rough surface before the release experiments. At the end of the release experiments, it was observed that the DLPMs maintained their spherical shape, but their surfaces were rougher with some defects, as shown in Fig. 6B and D. Since PCL is barely degraded without the proper solution or lipase and the morphology of the DLPMs didn't change obviously as observed by SEM, diffusion through the polymer was the only possible mechanism of drug release. Fig. 6C shows some irregularly shaped fragments near the DLPMs, and some DLPMs had a loose morphology, which means that the DLPMs showed degradation phenomena in PBS containing PS. Therefore, beside the diffusion mechanism, DLPMs in PBS containing PS demonstrated drug release through a degradation process.

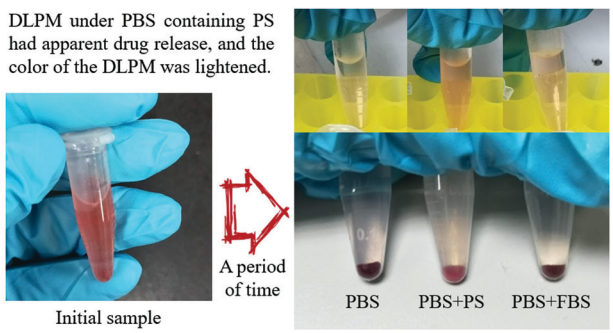

Fig. 5 Views of samples from the *in vitro* release experiments.

3.5. Molecular modelling approach

The compound–compound docking of doxorubicin hydrochloride with polycaprolactone showed potential binding affinity with −4.1 kcal mol^{-1} binding energy. Polycaprolactone showed a non-classical hydrogen bond between doxorubicin hydrochloride and oxygen (O), with a distance of 2.5 Å (Fig. 7).

3.6. Molecular dynamics simulations

Further, based on the docking scores of polycaprolactone and doxorubicin hydrochloride, the performed MD simulations were shown to demonstrate noble stability between 5–10 Å RMSD, observed during the simulations (50 nanoseconds); polycaprolactone and doxorubicin hydrochloride RMSD values, the radius of gyration and H-bond analysis of the complex are shown in Fig. 8 in 5 clusters (10 ns each) for a better understanding of the fluctuations. RMSD values, H-bonds and the radius of gyration were observed to show the best stability in cluster 5.

3.7. Histogram analysis of RMSD, radius of gyration and H-bond values

Fig. S4 (ESI†) (panel A) shows different histograms demonstrating RMSD analysis for the polycaprolactone and doxorubicin hydrochloride compounds over 10 ns in 5 clusters (50 ns). These were shown to possess noble stability between a frequency of 0.1 and 0.30, observed during the simulations (30–50 nanoseconds). Panel B indicates different histograms of MD simulation (radius of gyration) analysis of the polycaprolactone and doxorubicin hydrochloride compounds over 10 ns in 5 clusters (50 ns). These were shown to possess noble stability between a frequency of 0.1 and 0.30, observed during the simulations (35–50 nanosecond). Panel C indicates different histograms of MD simulation (H-bond) analysis of the polycaprolactone and doxorubicin hydrochloride compounds over 10 ns in 5 clusters (50 ns). These were shown to possess noble stability between a frequency of 0.1 and 1.6, as observed during simulations and shown in the ESI† (Fig. S4).

3.8. Polar analysis of RMSD, radius of gyration and H-bond values

As indicated in Fig. 9 (panel A), different polar representations were obtained of the MD simulation (RMSD) analysis for the polycaprolactone and doxorubicin hydrochloride compounds over 10 ns for 5 clusters. These were shown to possess noble stability between 0.1 and 0.6 (degrees), as observed during simulations. Fig. 9 (panel B) indicates different polar representations of the MD simulation (radius of gyration) analysis for the polycaprolactone and doxorubicin hydrochloride compounds over 10 ns in 5 clusters. These were shown to possess noble stability between 0.1 and 0.4 (degrees), as observed during simulations. Panel C indicates MD simulation (H-bond) analysis for the polycaprolactone and doxorubicin hydrochloride compounds over 10 ns in 5 clusters. These were recorded to possess noble stability between

 This journal is © The Royal Society of Chemistry and the Centre National de la Recherche Scientifique 2019

Published on 24 June 2019. Downloaded by National Sun Yat Sen University on 3/23/2020 10:57:07 AM.

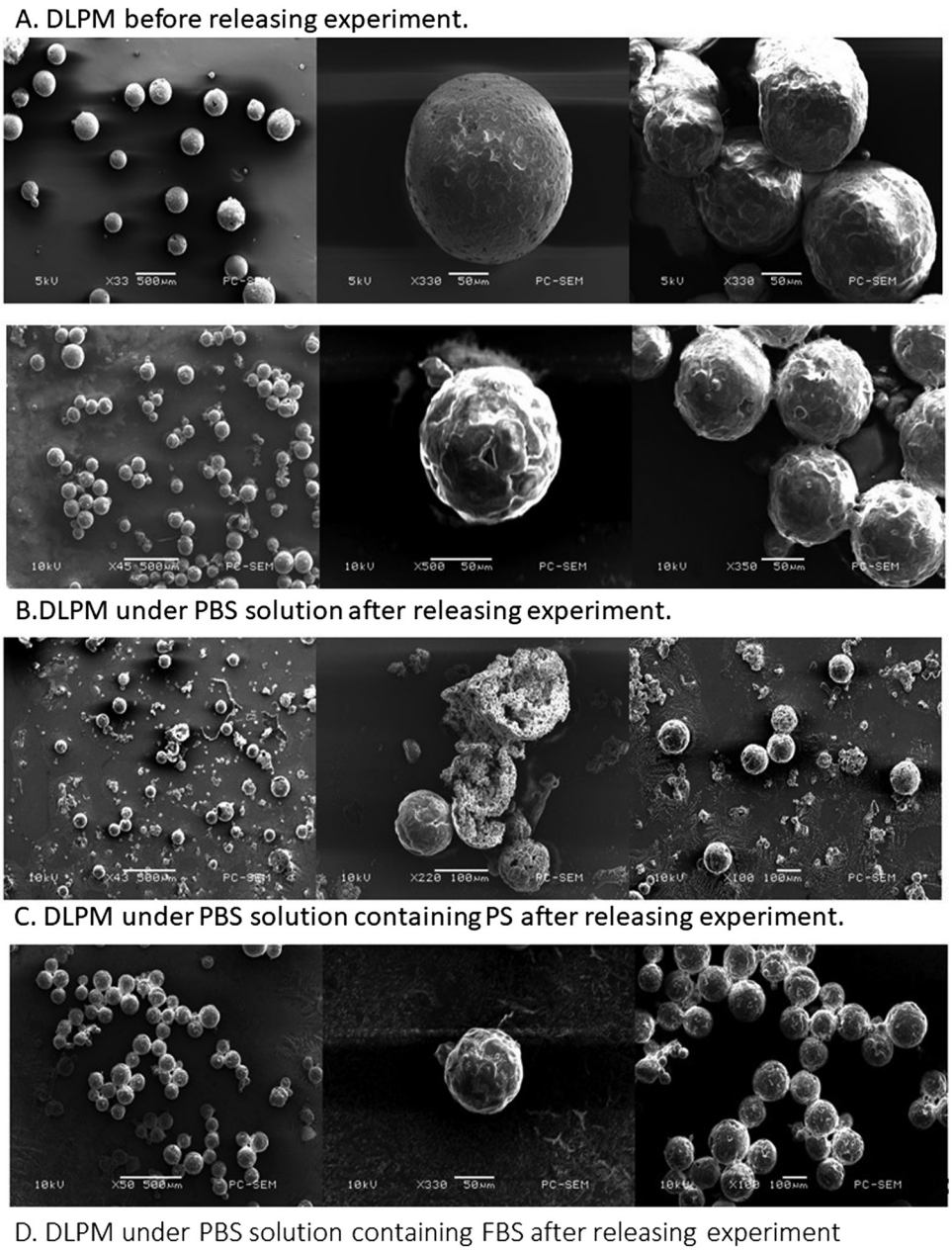

Fig. 6 *In vitro* release experiment SEM image profiles of DLPMs.

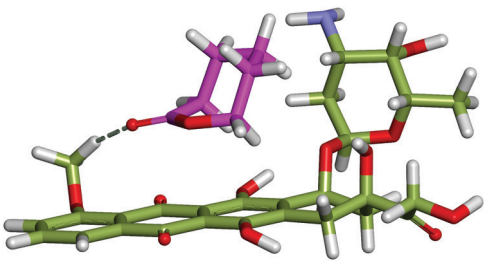

Fig. 7 A representation of polycaprolactone's (magenta) interaction with doxorubicin hydrochloride (light green).

0.1 and 0.2 (degrees) as observed during the simulations and shown in Fig. 9.

3.9. Comparative analysis of the radius of gyration and RMSD values

The radius of gyration and RMSD values for the polycaprolactone and doxorubicin hydrochloride compounds over 10 ns in 5 clusters were recorded to possess noble stability between 4 Å and 20 Å, as observed during simulations and shown in Fig. 10.

3.10. Correlation coefficient heat map analysis

A correlation coefficient heat map representation of the radius of gyration and RMSD values for the polycaprolactone and doxorubicin hydrochloride compounds over 10 ns in 5 clusters was shown to possess noble stability between 0.4 and 1.0, as observed during simulations (10–25 ns), but during the

Published on 24 June 2019. Downloaded by National Sun Yat Sen University on 3/23/2020 10:57:07 AM.

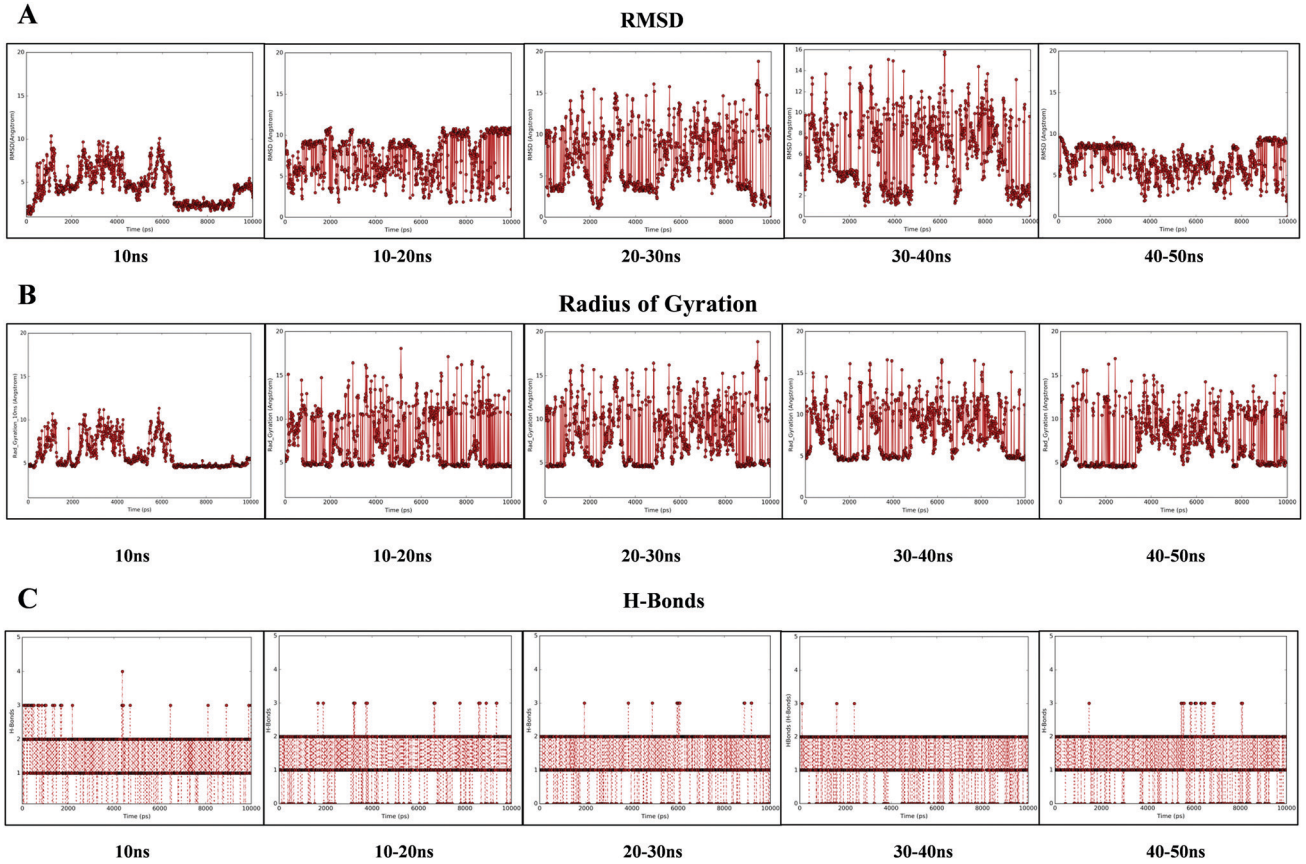

Fig. 8 (A) Indicates different curves representing MD simulation (RMSD) analysis of the polycaprolactone and doxorubicin hydrochloride compounds over 10 ns in 5 clusters. The *x*-axis represents the time in nanoseconds (50 ns) and the *y*-axis represents the RMSD in Ångstroms (Å). (B) Indicates different curves representing MD simulation (radius of gyration) analysis of the polycaprolactone and doxorubicin hydrochloride compounds over 10 ns in 5 clusters. The *x*-axis represents the time in nanoseconds (50 ns) and the *y*-axis represents the radius of gyration in Ångstroms (Å). (C) Indicates MD simulation (H-bond) analysis of the polycaprolactone and doxorubicin hydrochloride compounds over 10 ns in 5 clusters. The *x*-axis represents the time in nanoseconds (50 ns) and the *y*-axis represents the number of H-bonds.

production phase, the stable time was 25–50 ns, as shown in the ESI† (Fig. S5).

3.11. Torsion analysis of polycaprolactone and doxorubicin hydrochloride using molecular dynamics simulations

During 50 ns of simulation, we observed that torsion is more stable after 30–50 ns of simulation. Initially, the polycaprolactone and doxorubicin hydrochloride bonding was more flexible. The top panel of Fig. 11 (Section A) represents polycaprolactone torsion ($C_6H_{10}O_2$), which was recorded to possess noble stability between 0.1 and 90 degrees, as observed during the initial simulation, but during the production phase, the stable time was 50 nanoseconds. The lower panel represents the doxorubicin hydrochloride torsion ($C_{27}H_{30}ClNO_{11}$), which was recorded to possess noble stability between 0.1 and 180 degrees, as observed during initial simulations, but during the production phase, the stable time was 50 ns. In Fig. 11 panel A, the light blue color represents polycaprolactone torsion ($C_6H_{10}O_2$), the circle indicates the degree of polycaprolactone torsion and the bars indicates the degree of polycaprolactone torsion in histogram form; while the bottom panel represents doxorubicin hydrochloride torsion ($C_{27}H_{30}ClNO_{11}$), where A and B (blue and pink colors) indicate carbon, C and D (purple and red colors) indicate hydrogen, E and F (dark blue and light green colors) indicate chlorine, G and H (yellow and dark green colors) indicate nitrogen, and I and J (orange and chocolate color) indicate oxygen torsion.

3.12. Systems biology approach

Also known as acute lymphoid leukemia, acute lymphoblastic leukemia (ALL) is a type of cancer that affects platelets, red blood cells, and white blood cells. It is typically associated with blood and bone marrow and is common among children. This type of cancer is initiated when lymphoblasts, a type of blood stem cell, begin to function abnormally. This abnormality leads to the development of large numbers of immature lymphocytes, which are unable to help the body to fight against foreign agents. If it is not diagnosed and treated quickly, within weeks, immature lymphocytes can overcrowd the bone marrow. This leads to a prevention of the distribution and flow of nutrients to blood cells. Typical signs and symptoms of ALL include anemia, dizziness, bleeding from the gums, bone and joint pain, bruising, fever, testicular enlargement, and enlarged lymph nodes. This type of cancer can be treated with chemotherapy or with drugs that can specifically destroy cancerous cells.

 This journal is © The Royal Society of Chemistry and the Centre National de la Recherche Scientifique 2019

Published on 24 June 2019. Downloaded by National Sun Yat Sen University on 3/23/2020 10:57:07 AM.

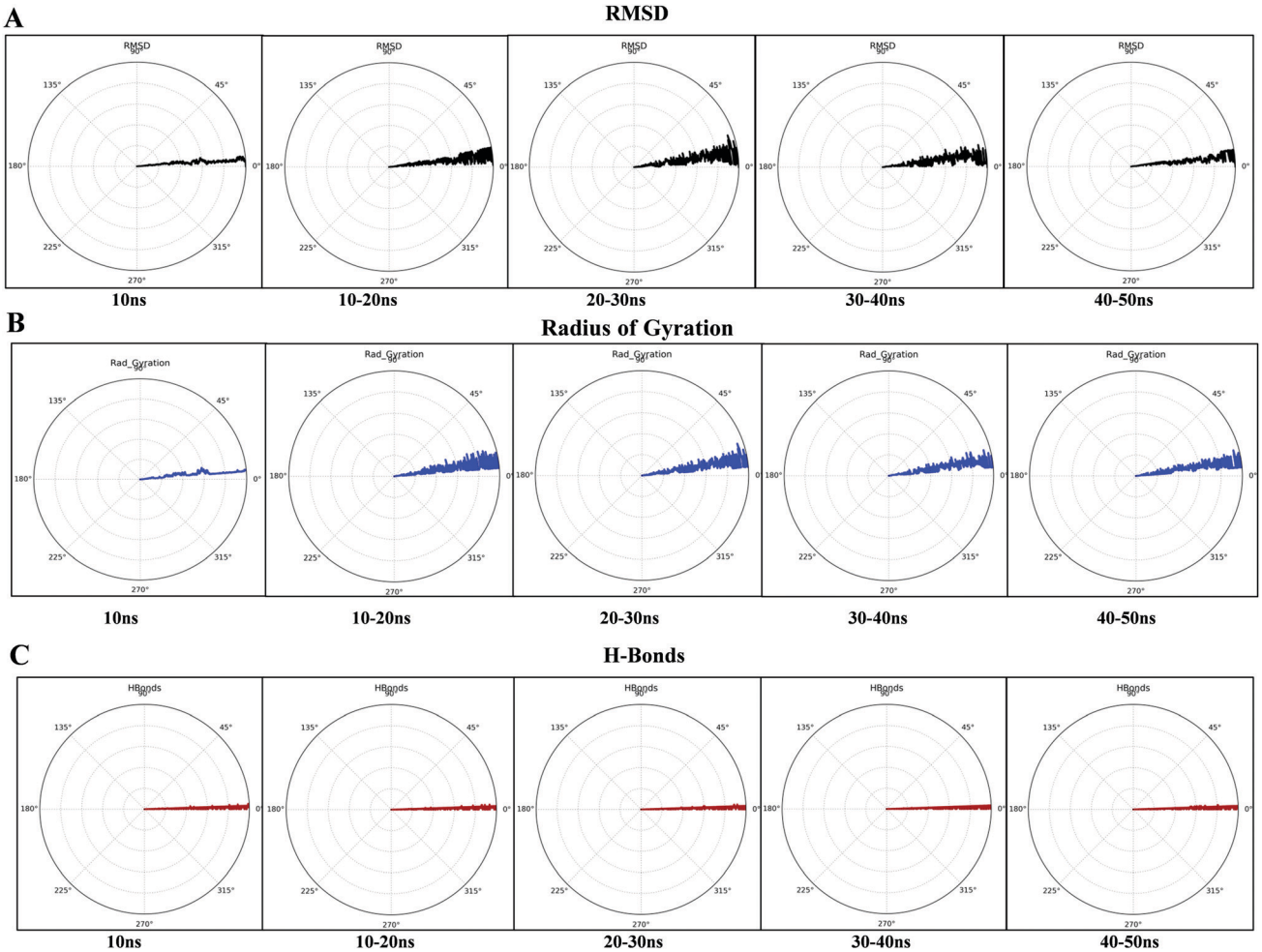

Fig. 9 (A) Indicates MD simulation (RMSD) analysis of the polycaprolactone and doxorubicin hydrochloride compounds over 10 ns in 5 clusters. The *x*-axis represents the time in nanoseconds (50 ns) and the *y*-axis represents degrees. (B) Indicates different polar representations of the MD simulation (radius of gyration) analysis of the polycaprolactone and doxorubicin hydrochloride compounds over 10 ns in 5 clusters. The *x*-axis represents the time in nanoseconds (50 ns) and the *y*-axis represents degrees. (C) Indicates MD simulation (H-bond) analysis of the polycaprolactone and doxorubicin hydrochloride compounds over 10 ns in 5 clusters. The *x*-axis represents the time in nanoseconds (50 ns) and the *y*-axis represents degrees.

In addition to chemotherapy, radiation therapy and stem cell transplantation can also be used as treatments. For our research, a literature survey was carried out with the aim of identifying and gleaning the necessary information regarding acute lymphoblastic/myeloid leukemia. Apart from this, a pharmacokinetics pathway was also created to ascertain the efficacy of our drug (0.47 μm). While the nodes in the pathway represent entities, the edges denote node connectivity. Pharmacokinetics studies were carried out with concentrated doses of 0.47 μm, as shown in Fig. 12.

To investigate the relationships, mechanisms, and interactions between biological organizations, it is pertinent to use biological network representations. Moreover, the pharmacokinetic mechanism of acute lymphoblastic/myeloid leukemia has been investigated using biochemical mathematical theories and models. In the presence of the nano-drug, the system was stabilized, as shown in Fig. 13, illustrating the pharmacokinetics simulation when there is a high risk of acute lymphoblastic/myeloid leukemia. Similar results were also obtained with an experimentally reported concentration.

3.13. A systems biology approach to validate the potential nano-drug activity in entire systems for a predicted *in silico* biochemical pathway of acute lymphoblastic/myeloid leukemia

3.13.1 Ordinary differential equations (ODEs) to model the nano-drug concentration. Nano-drug injections can be modeled over time through ordinary differential equations (ODEs) *via* a systems biology approach, starting off with the equations

$$d([\text{acute lymphoblastic solid}])/dt = -\text{ReactionFlux1}$$

$$d([\text{acute lymphoblastic tritur}])/dt = \text{ReactionFlux1} - \text{ReactionFlux2}$$

$$d([\text{acute lymphoblastic}])/dt = \text{ReactionFlux2} - \text{ReactionFlux3}$$

$$d([[\text{plasma acute lymphoblastic}]])/dt = \text{ReactionFlux4} - \text{ReactionFlux5} + \text{ReactionFlux6} - \text{ReactionFlux8} - \text{ReactionFlux9}$$

$$d([\text{tissue acute lymphoblastic}])/dt = \text{ReactionFlux5} - \text{ReactionFlux7}$$

Published on 24 June 2019. Downloaded by National Sun Yat Sen University on 3/23/2020 10:57:07 AM.

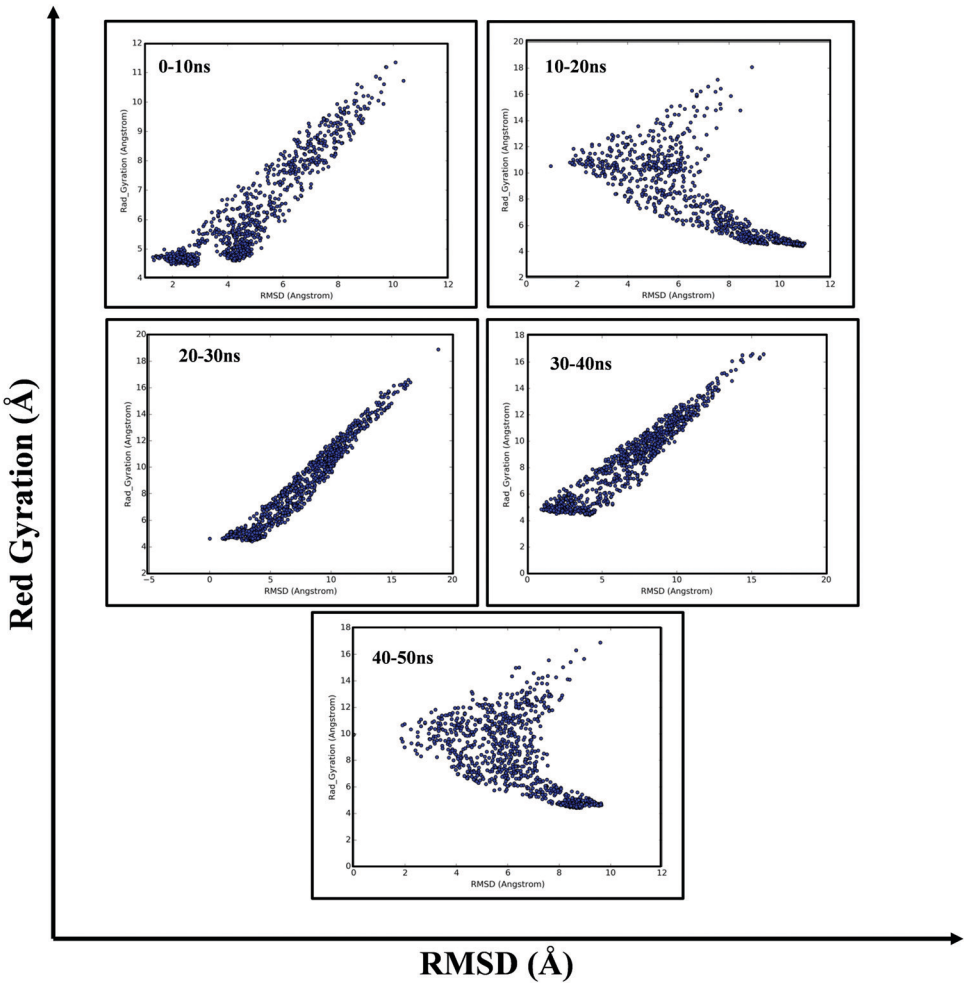

Fig. 10 Diagonal representations of the radius of gyration and RMSD values for the polycaprolactone and doxorubicin hydrochloride compounds over 10 ns in 5 clusters. The *x*-axis represents the RMSD values in Ångstroms (Å) and the *y*-axis represents the radius of gyration values in Ångstroms (Å).

$$\mathrm{d}([\text{Blood acute lymphoblastic}])/\mathrm{d}t = 1/\text{acute lymphoblastic} \times (\text{ReactionFlux16} - \text{ReactionFlux17})$$

$$\mathrm{d}([\text{portal acute lymphoblastic}])/\mathrm{d}t = \text{ReactionFlux10} - \text{ReactionFlux11}$$

$$\mathrm{d}([\text{liver acute lymphoblastic}])/\mathrm{d}t = \text{ReactionFlux11} - \text{ReactionFlux12} - \text{ReactionFlux13}$$

$$\mathrm{d}([\text{plasma acute lymphoblastic}])/\mathrm{d}t = \text{ReactionFlux12} - \text{ReactionFlux14}$$

$$\mathrm{d}([\text{acute lymphoblastic delay 1}])/\mathrm{d}t = 1/\text{acute lymphoblastic} \times (\text{ReactionFlux15} - \text{ReactionFlux18})$$

$$\mathrm{d}([\text{acute lymphoblastic delay 2}])/\mathrm{d}t = 1/\text{acute lymphoblastic} \times (\text{ReactionFlux18} - \text{ReactionFlux19})$$

$$\mathrm{d}([\text{plasma acute lymphoblastic nano-drug conc}])/\mathrm{d}t = [\text{plasma acute lymphoblastic nano-drug conc rate}]$$

3.13.2 Repeated assignments. The given ODEs depict that the amount of nano-drug in the bloodstream is changing over a period of time while injections of the drug are discrete. Here we try to transform this into a function

$$[\text{plasma acute lymphoblastic nano-drug conc}] = [\text{plasma acute lymphoblastic nano-drug}] / [\text{plasma volume (acute lymphoblastic nano-drug)}]$$

$$[\text{acute lymphoblastic nano-drug secr}] = \text{cell} \times [\text{portal acute lymphoblastic nano-drug}]$$

$$[\text{hepatic extraction}] = -m5 \times [\text{acute lymphoblastic nano-drug secr}] + m6$$

$$m3 = [\text{hepatic extraction}] \times m1/(1 - [\text{hepatic extraction}])$$

$$[\text{acute lymphoblastic nano-drug excretion}] = ([\text{acute lymphoblastic nano-drug excretion mode}] = 1) \times \text{ke1} \times ([\text{plasma acute lymphoblastic nano-drug}] - \text{ke2})$$

 This journal is © The Royal Society of Chemistry and the Centre National de la Recherche Scientifique 2019

Published on 24 June 2019. Downloaded by National Sun Yat Sen University on 3/23/2020 10:57:07 AM.

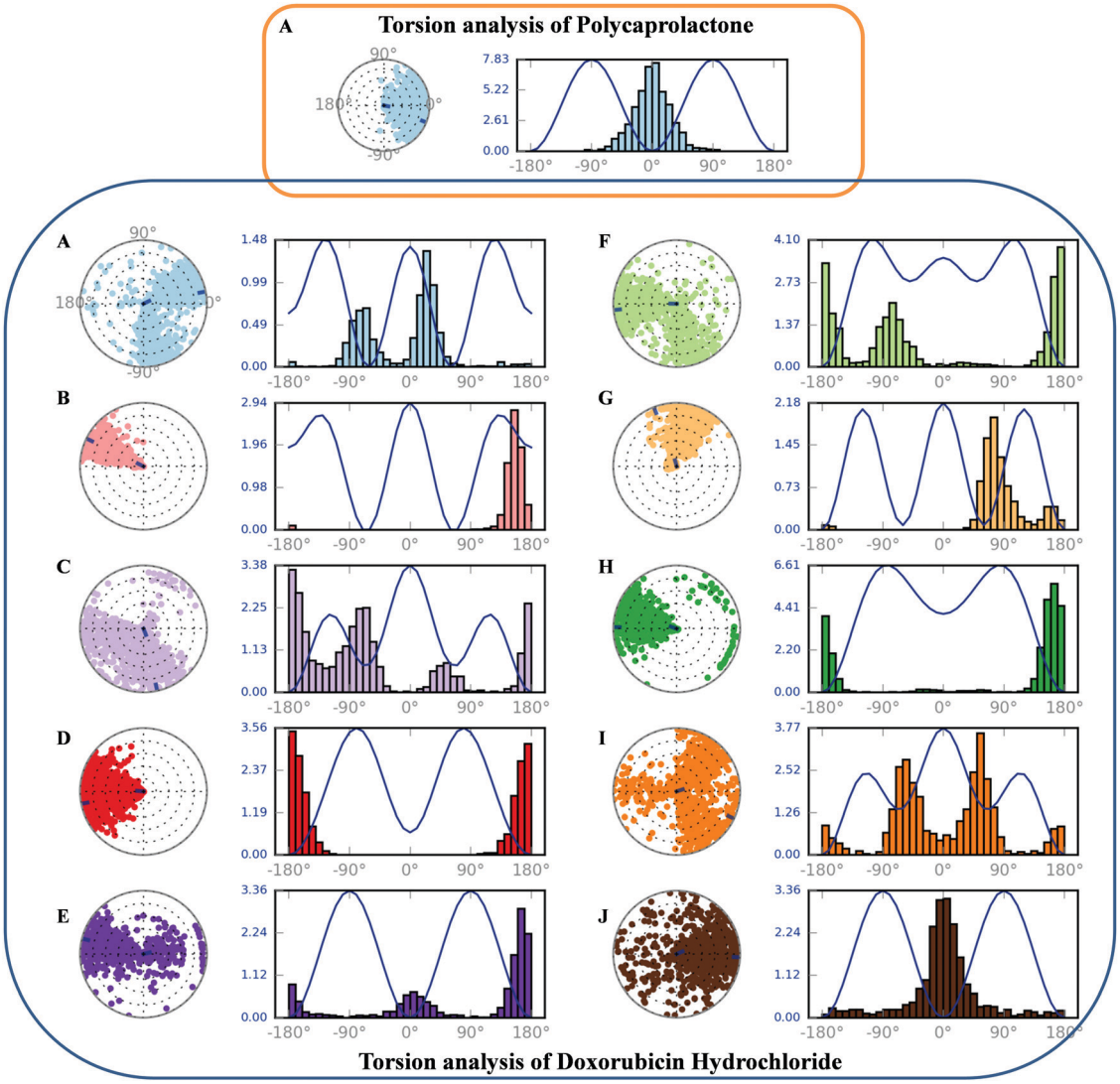

Fig. 11 Torsion representations of polycaprolactone and doxorubicin hydrochloride, where the *x*-axis represents degrees and the *y*-axis represents the torsion of atoms in Ångstroms (Å). The top panel of this figure (panel A, light blue color) represents polycaprolactone torsion ($C_6H_{10}O_2$), the circle indicates the degree of polycaprolactone torsion and the bars indicate the degree of polycaprolactone torsion in histogram form. The bottom panel represents doxorubicin hydrochloride torsion ($C_{27}H_{30}ClNO_{11}$), with torsion of different atoms as follows: A and B: carbon; C and D: hydrogen; E and F: chlorine; G and H: nitrogen; I and J: oxygen.

$$V_m = V_m^0 + V_{max}\text{*[acute lymphoblastic nano-drug]}$$

$$\text{[acute lymphoblastic dep nano-drug util]} = V_m\text{*[tissue nano-drug]}/(K_m + \text{[tissue nano-drug]})$$

$$\text{[nano-drug util]} = \text{[acute lymphoblastic ind nano-drug util]} + \text{[acute lymphoblastic dep nano-drug util]}$$

$$\text{[nano-drug appear rate]} = f \times k_{abs} \times \text{[gut nano-drug]} \times \left(\frac{\text{basis}}{\text{[body weight]}}\right)$$

$$\text{[nano-drug prod]} = \text{kp1} - \text{kp2} \times \text{[plasma nano-drug]} - \text{kp3} \times \text{[acute lymphoblastic delay 2]} - \text{kp4} \times \text{[portal acute lymphoblastic]}$$

$$\text{plasma nano-drug conc rate]} = (\text{[nano-drug prod]} + \text{[nano-drug appear rate]} - \text{[acute lymphoblastic ind nano-drug util]} - \text{[nano-drug excretion]} - k1 \times \text{[plasma nano-drug]} + k2 \times \text{[tissue nano-drug]})/\text{[plasma volume(nano-drug)]}$$

$$\text{[acute lymphoblastic prod]} = \text{[delayed nano-drug signal]} + \text{[basal acute lymphoblastic nano-drug secr]} + (\text{[acute lymphoblastic prod mode]} = 1) \times K \times \text{[plasma nano-drug conc rate]}$$

$$\text{[stomach nano-drug]} = \text{[stomach nano-drug solid]} + \text{[stomach nano-drug tritur]}$$

Published on 24 June 2019. Downloaded by National Sun Yat Sen University on 3/23/2020 10:57:07 AM.

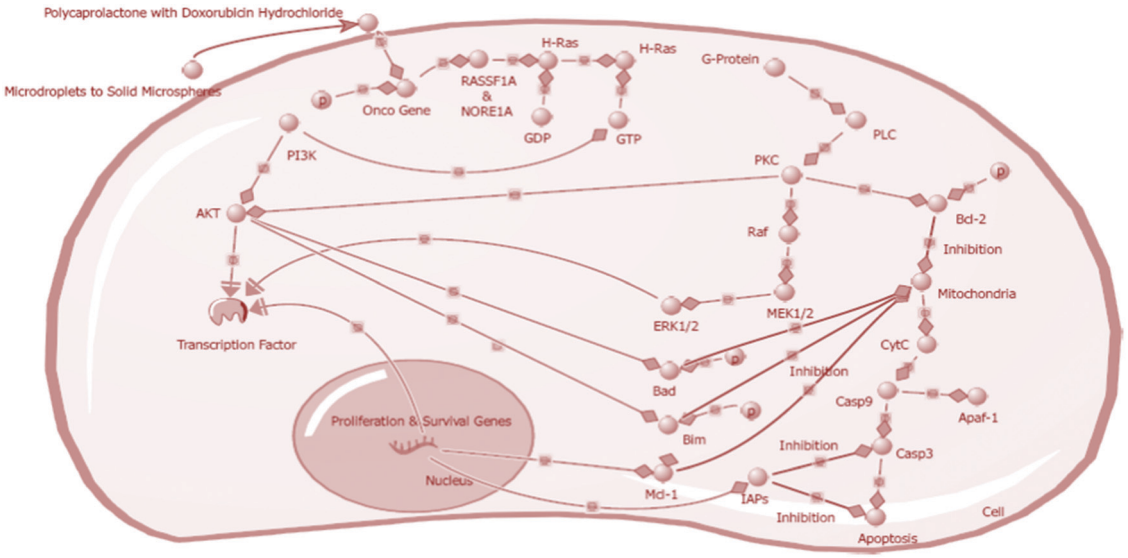

Fig. 12 A representation of the biochemical pathway of liver cancer in the presence of polycaprolactone interactions with doxorubicin hydrochloride.

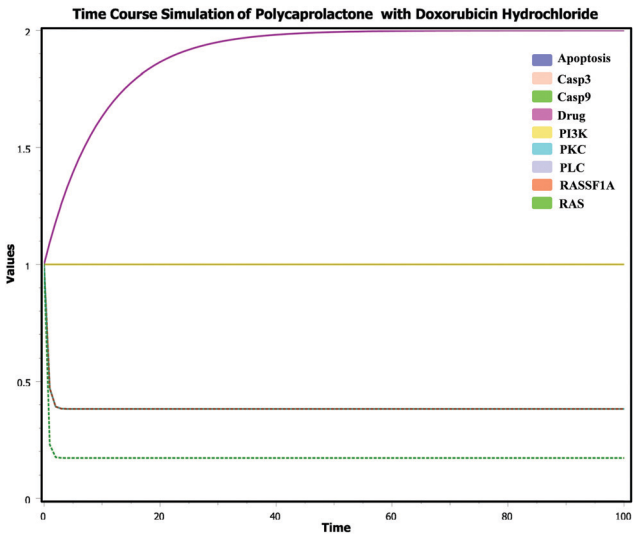

Fig. 13 A representation of a time course simulation of the entire pathway in the presence of the interaction of polycaprolactone with doxorubicin hydrochloride.

$$k_{empt} = k_{min} + 0.5 \times (k_{max} - k_{min}) \times (\tanh(a \times ([\text{stomach nano-drug}] - b \times [\text{stomach nano-drug after dosing}])) - \tanh(c \times ([\text{stomach nano-drug}] - d \times [\text{stomach nano-drug after dosing}])) + 2)$$

3.13.3 Parameter values. Pharmacodynamic parameters and values refer to the drug concentration at the site of action with resulting effects, which also includes the time course and the intensity of therapeutic and adverse effects.

3.14. Time course simulations

The antigenic potential of the drug was confirmed using an *in silico* biochemical pathway of acute lymphoblastic/myeloid leukemia, which, in turn, was designed using a systems biology workbench of computational systems and through different literature surveys related to systems biology.[70–77] Also used for demonstrating the sufficiency as well as the appropriateness of the tested drug are kinetics simulations or pharmacokinetics simulations. At therapeutic doses, most drug pharmacokinetics involve first-order reactions that can be solved using the Michaelis–Menten equation or mass kinetics equations to demonstrate non-linear kinetics schemes. Time course simulations were carried out in the presence of the nano-drug (depicted by the pink peak in Fig. 13), which indicated its effective role in the predicted *in silico* biochemical pathway of acute lymphoblastic/myeloid leukemia, while oncogenes and oncogene cycles were down-regulated during the simulation, as shown in the ESI† (Fig. S6).

3.15. Stochastic simulations

The interactions and mechanisms between entities can be explained *via* representations of biological networks. The pharmacokinetic mode of operation of lymphoblastic leukemia can be studied using biochemical models (Fig. 13). Reports from experimental studies have also shown the adverse effects of lymphoblastic leukemia. What's more, similar results have been obtained with this concentration, as reported in other experiments. The down-regulation of entities is shown in the graph and this trend indicates the inhibition of acute lymphoblastic/myeloid leukemia (Fig. 13).

3.16. Cell line analysis

The DOX-loaded PCL microspheres were added into cells in medium at 1 mg mL^{-1}, with the same weight for both small (20–100 μm) and large (100–200 μm) DLPMs. Therefore, the particle number of small DLPMs (~1057) is more than that of large (~785) DLPMs. Also, small DLPMs have a larger total surface area compared to large DLPMs at the same weight (1 mg). Therefore, within CCRF-CEM cells, small DLPMs killed more cells compared to large ones (Fig. 14). Generally, DLPMs

 This journal is © The Royal Society of Chemistry and the Centre National de la Recherche Scientifique 2019

Published on 24 June 2019. Downloaded by National Sun Yat Sen University on 3/23/2020 10:57:07 AM.

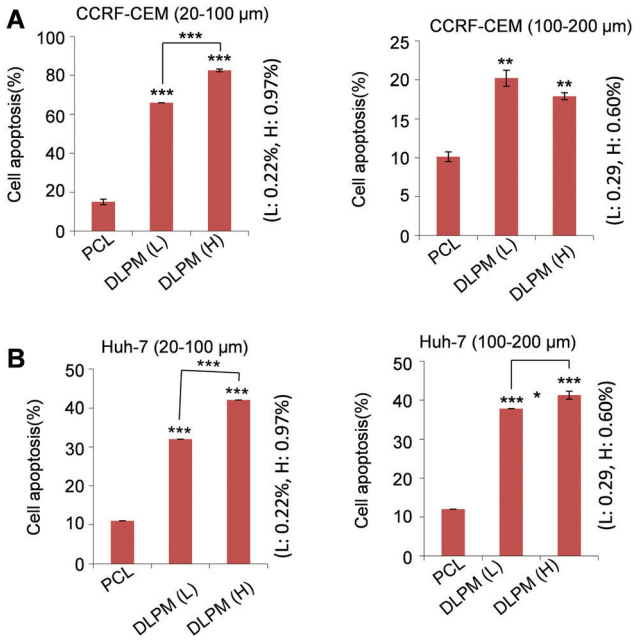

Fig. 14 DOX-loaded PCL microspheres induce apoptosis in two distinct cancer cell lines, CCRF-CEM and Huh-7. After treatment with DOX-loaded PCL microspheres (DLPMs; 1 mg mL^{-1}) for 48 h, flow cytometric analysis identified that DLPMs with low (L) and high (H) encapsulation efficiencies, accompanied by different sizes (20–100 μm and 100–200 μm), induced apoptosis in (A) CCRF-CEM and (B) Huh-7 cells. All experiments were performed in triplicate and results are expressed as mean values ± SEM. Statistical significance: *: $P < 0.05$; **: $P < 0.01$; ***: $P < 0.001$.

with high encapsulation efficiency at different diameters induced profound apoptosis in both cell lines. In a suspension of CCRF-CEM cells, small DLPMs induced a higher apoptotic rate (66.0–82.5%) compared to large DLPMs (17.9–20.2%) (Fig. 14). Also, in comparison with large ones, small DLPMs retain a relatively high surface area; accordingly, a suspension of CCRF-CEM cells was evenly surrounded by DLPMs releasing DOX. On the other hand, small and large DLPMs induced similar apoptotic rates (32.0–41.3%) in adherent Huh-7 cells (Fig. 14), perhaps due to the exposure of only one side of the cell surface to DLPMs releasing DOX. Our results suggest that DLPMs can induce apoptosis effectively in both suspensions and adherent cells within 48 h.

4. Conclusions

It can be concluded that this study attempted to obtain and successfully developed biodegradable polycaprolactone (PCL) microspheres of uniform particle size having low material loss, through emulsification assisted by an ultrasonic atomization (EUA) method for mass production. We used a high frequency (~43 kHz) vibrating surface on an ultrasonic nozzle to break a thin liquid film of PCL oil solution and, further, uniform PCL microdroplets (particle size: ~20–55 μm) were sprayed out softly and directly. From the results of PCL degradation and *in vitro* release experiments, about 10% of the weight of the microspheres was lost in one months in PBS solution at 37 °C. The DLPM morphology didn't change obviously in PBS and PBS containing FBS, as studied *via* SEM. Therefore, the release within two weeks was judged as the continuous diffusion of DOX from the microspheres. In PBS containing pseudomonas lipase (PS), we found the morphology of the DLPMs to be loose after the release experiments. Among enzymes, PS has the property of degrading PCL, making DLPM release ~70% of the drug in two weeks. We also successfully carried out predictions involving the binding site region to investigate the binding region responsible for the interaction of polycaprolactone with doxorubicin hydrochloride and its activation, which, in turn, inhibits liver cancer. Further, we performed docking and MD simulations of the polycaprolactone and doxorubicin hydrochloride interaction that showed their binding affinity and were later validated. Additionally, we have successfully established the dynamic behavior of an entire biochemical pathway in the presence of polycaprolactone with doxorubicin hydrochloride using a systems biology approach.

Authors contributions

Conceptualization: ACK, AK, CTP; data curation: ACK; formal analysis: ACK, AK, SPS, CYY, SWK, SSL, XW, YJW, CKY, XD, CTP, YLS; funding acquisition: DQW; investigation: DQW, ACK; methodology: ACK, AK, CTP; project administration: DQW, SS; resources: ACK, DQW; supervision: YLS, DQW; validation: ACK, AK, SPS, CYY, SWK, SSL, XW, YJW, CKY, XD, CTP, YLS, DQW; writing-original draft: ACK, AK; writing-review draft: ACK, AK, SPS, CYY, SWK, SSL, XW, YJW, CKY, XD, CTP, YLS.

Conflicts of interest

We declare no competing interests.

Acknowledgements

This work was financially supported by the Ministry of Science & Technology, Taiwan, under contra MOST 107-2221-E-110-031-MY3 and 107-2221-E-110-032-MY3. This work is supported by the grants from the Key Research Area Grant 2016YFA0501703 and 2018ZX10302205-004-002 of the Ministry of Science and Technology of China, the National Natural Science Foundation of China (Contract no. 61832019, 61503244 and BK20161130), the State Key Lab of Microbial Metabolism and Joint Research Funds for Medical and Engineering and Scientific Research at Shanghai Jiao Tong University (YG2017ZD14).The Six Talent Peaks Project in Jiangsu Province (grant number: SWYY-128), Postgraduate Education Reform Project of Jiangsu Province, and Research Funds for the Medical School of Jiangnan University ESI special cultivation project (grant number: 1286010241170320).

References

1 A. Forner, M. Reig and J. Bruix, Hepatocellular carcinoma, *Lancet*, 2018, **391**, 1301–1314.
2 K. J. Lafaro, A. N. Demirjian and T. M. Pawlik, Epidemiology of Hepatocellular Carcinoma, *Surgical Oncology Clinics of North America*, 2015, **24**, 1–17.

Published on 24 June 2019. Downloaded by National Sun Yat Sen University on 3/23/2020 10:57:07 AM.

3 J. M. Llovet and J. Bruix, Novel advancements in the management of hepatocellular carcinoma in 2008, *J. Hepatol.*, 2008, **48**, S20–S37.
4 M.-A. Buendia and C. Neuveut, Hepatocellular carcinoma, *Cold Spring Harbor Perspect. Med.*, 2015, **5**, a021444.
5 M. G. Refolo, *et al.*, Chlorogenic acid improves the regorafenib effects in human hepatocellular carcinoma cells, *Int. J. Mol. Sci.*, 2018, **19**(5), 1518.
6 T. H. Chu, *et al.*, Celecoxib enhances the therapeutic efficacy of epirubicin for Novikoff hepatoma in rats, *Cancer Med.*, 2018, **7**, 2567–2580.
7 K. Xu, *et al.*, Nanomaterials in the Prevention, Diagnosis, and Treatment of Mycobacterium Tuberculosis Infections, *Adv. Healthcare Mater.*, 2018, **7**(1), 1700509.
8 M. Rastegar, *et al.*, Investigating effect of rapamycin and metformin on angiogenesis in hepatocellular carcinoma cell line, *Adv. Pharm. Bull.*, 2018, **8**(1), 63.
9 J. Bruix and M. Sherman, Management of hepatocellular carcinoma: An update, *Hepatology*, 2011, **53**, 1020–1022.
10 E. S. Bialecki and A. M. Di Bisceglie, Diagnosis of hepatocellular carcinoma, *HPB*, 2005, **7**(1), 26–34.
11 J. Berumen and A. Hemming, Liver transplantation for hepatocellular carcinoma, *Abdom. Radiol.*, 2018, **43**(1), 185–192.
12 H. B. El-Serag and K. L. Rudolph, Hepatocellular Carcinoma: Epidemiology and Molecular Carcinogenesis, *Gastroenterology*, 2007, **132**(7), 2557–2576.
13 J. M. Llovet, *et al.*, Design and endpoints of clinical trials in hepatocellular carcinoma, *J. Natl. Cancer Inst.*, 2008, **100**(10), 698–711.
14 S. H. Wang, S. H. Yeh and P. J. Chen, Hepatocellular carcinoma and hepatitis C virus, *Hepatitis C Virus II: Infection and Disease*, 2016, ISBN: 978-4-431-56101-9.
15 A. Hoshino, *et al.*, Tumour exosome integrins determine organotropic metastasis, *Nature*, 2015, **527**(7578), 329.
16 F. D. S. e Melo, *et al.*, A distinct role for Lgr5+ stem cells in primary and metastatic colon cancer, *Nature*, 2017, **543**(7647), 676.
17 C. Penna and B. Nordlinger, Colorectal metastasis (liver and lung), *Surgical Clinics of North America*, 2002, **82**(5), 1075–1090.
18 K. Hur, *et al.*, MicroRNA-200c modulates epithelial-tomesenchymal transition (EMT) in human colorectal cancer metastasis, *Gut*, 2013, **62**(9), 1315–1326.
19 J. M. Loo, *et al.*, Extracellular metabolic energetics can promote cancer progression, *Cell*, 2015, **160**(3), 393–406.
20 K. Liang, J. E. Chung, S. J. Gao, N. Yongvongsoontorn and M. Kurisawa, Highly Augmented Drug Loading and Stability of Micellar Nanocomplexes Composed of Doxorubicin and Poly(ethylene glycol)–Green Tea Catechin Conjugate for Cancer Therapy, *Adv. Mater.*, 2018, **30**(14), 1706963.
21 S. Li, *et al.*, Quercetin reversed MDR in breast cancer cells through down-regulating P-gp expression and eliminating cancer stem cells mediated by YB-1 nuclear translocation, *Phyther. Res.*, 2018, **32**(8), 1530–1536.
22 D. Diaz-Diestra, B. Thapa, D. Badillo-Diaz and J. Beltran-Huarac, Graphene Oxide/ZnS:Mn Nanocomposite Functionalized with Folic Acid as a Nontoxic and Effective Theranostic Platform for Breast Cancer Treatment, *Nanomaterials*, 2018, **8**(7), 484.
23 A. C. Kaushik and S. Sahi, Boolean network model for GPR142 against Type 2 diabetes and relative dynamic change ratio analysis using systems and biological circuits approach, *Syst. Synth. Biol.*, 2015, **9**, 45–54.
24 A. C. Kaushik, *et al.*, G-protein-coupled receptors function as logic gates for nanoparticle binding using systems and synthetic biology approach, *J. Mater. Res.*, 2019, 1–14.
25 A. C. Kaushik, *et al.*, Deciphering G-Protein-Coupled Receptor 119 Agonists as Promising Strategy against Type 2 Diabetes Using Systems Biology Approach, *ACS Omega*, 2018, **3**, 18214–18226.
26 K. T. Brown, *et al.*, Randomized trial of hepatic artery embolization for hepatocellular carcinoma using doxorubicin-eluting microspheres compared with embolization with microspheres alone, *J. Clin. Oncol.*, 2016, **34**(17), 2046.
27 M. Bendszus, *et al.*, Efficacy of trisacryl gelatin microspheres versus polyvinyl alcohol particles in the preoperative embolization of meningiomas, *AJNR. Am. J. Neuroradiol.*, 2000, **21**(2), 255–261.
28 K. Fuchs, *et al.*, Drug-eluting beads loaded with anti-angiogenic agents for chemoembolization: In vitro sunitinib loading and release and in vivo pharmacokinetics in an animal model, *J. Vasc. Interv. Radiol.*, 2014, **25**(3), 379–387.
29 T. J. Ward, *et al.*, Management of high hepatopulmonary shunting in patients undergoing hepatic radioembolization, *J. Vasc. Interv. Radiol.*, 2015, **26**(12), 1751–1760.
30 O. Suwantong, Biomedical applications of electrospun polycaprolactone fiber mats, *Polym. Adv. Technol.*, 2016, **27**(10), 1264–1273.
31 Y. He, *et al.*, A new photocrosslinkable polycaprolactone-based ink for three-dimensional inkjet printing, *J. Biomed. Mater. Res. - Part B Appl. Biomater.*, 2017, **105**(6), 1645–1657.
32 A. Ronca, *et al.*, Synthesis and characterization of divinyl-fumarate poly-ε-caprolactone for scaffolds with controlled architectures, *J. Tissue Eng. Regen. Med.*, 2018, **12**(1), e523–e531.
33 B. J. Kim, *et al.*, Accelerated skin wound healing using electrospun nanofibrous mats blended with mussel adhesive protein and polycaprolactone, *J. Biomed. Mater. Res. - Part A*, 2017, **105**(1), 218–225.
34 A. C. Kaushik, S. Kumar, D. Q. Wei and S. Sahi, Structure Based Virtual Screening Studies to Identify Novel Potential Compounds for GPR142 and Their Relative Dynamic Analysis for Study of Type 2 Diabetes, *Front. Chem.*, 2018, **6**, 23.
35 A. C. Kaushik, S. Bharadwaj, S. Kumar and D.-Q. Wei, Nanoparticle mediated inhibition of Parkinson's disease using computational biology approach, *Sci. Rep.*, 2018, **8**, 9169.
36 A. C. Kaushik, *et al.*, Evaluation and validation of synergistic effects of amyloid-beta inhibitor–gold nanoparticles complex on Alzheimer's disease using deep neural network approach, *J. Mater. Res.*, 2019, **34**(11), 1845–1853.
37 A. C. Kaushik, *et al.*, Deciphering the Biochemical Pathway and Pharmacokinetic Study of Amyloid βeta-42 with Superparamagnetic Iron Oxide Nanoparticles (SPIONs) Using Systems Biology Approach, *Mol. Neurobiol.*, 2018, **55**, 3224–3236.

Published on 24 June 2019. Downloaded by National Sun Yat Sen University on 3/23/2020 10:57:07 AM.

38 D. E. Robinson, *et al.*, Plasma Polymer and Biomolecule Modification of 3D Scaffolds for Tissue Engineering, *Plasma Process. Polym.*, 2016, **13**(7), 678–689.
39 K. H. Hsu, *et al.*, Hybrid Electrospun Polycaprolactone Mats Consisting of Nanofibers and Microbeads for Extended Release of Dexamethasone, *Pharm. Res.*, 2016, **33**(6), 1509–1516.
40 K. Mubyana, R. A. Koppes, K. L. Lee, J. A. Cooper and D. T. Corr, The influence of specimen thickness and alignment on the material and failure properties of electrospun polycaprolactone nanofiber mats, *J. Biomed. Mater. Res. - Part A*, 2016, **104**(11), 2794–2800.
41 T. Isono, *et al.*, Self-Assembly of Maltoheptaose-*block*-polycaprolactone Copolymers: Carbohydrate-Decorated Nanoparticles with Tunable Morphology and Size in Aqueous Media, *Macromolecules*, 2016, **49**(11), 4178–4194.
42 Q. Mei, *et al.*, Formulation and *in vitro* characterization of rifampicin-loaded porous poly (ε-caprolactone) microspheres for sustained skeletal delivery, *Drug Des. Devel. Ther.*, 2018, **12**, 1533.
43 R. Groynom, E. Shoffstall, L. S. Wu, R. H. Kramer and E. B. Lavik, Controlled release of photoswitch drugs by degradable polymer microspheres, *J. Drug Target.*, 2015, **23**(7–8), 710–715.
44 A. G. Sullad, L. S. Manjeshwar and T. M. Aminabhavi, Blend microspheres of chitosan and polyurethane for controlled release of water-soluble antihypertensitive drugs, *Polym. Bull.*, 2014, **72**(2), 265–280.
45 S. R. Abulateefeh and A. M. Alkilany, Synthesis and Characterization of PLGA Shell Microcapsules Containing Aqueous Cores Prepared by Internal Phase Separation, *AAPS PharmSciTech*, 2016, **17**(4), 891–897.
46 S. G. Kumbar and T. M. Aminabhavi, Synthesis and characterization of modified chitosan microspheres: Effect of the grafting ratio on the controlled release of nifedipine through microspheres, *J. Appl. Polym. Sci.*, 2003, **89**(11), 2940–2949.
47 D. Peng, K. Huang, Y. Liu and S. Liu, Preparation of novel polymeric microspheres for controlled release of finasteride, *Int. J. Pharm.*, 2007, **342**(1–2), 82–86.
48 A. Kremling and J. Saez-Rodriguez, Systems biology-An engineering perspective, *J. Biotechnol.*, 2007, **129**(2), 329–351.
49 T. Iba, An autopoietic systems theory for creativity, *Procedia - Social and Behavioral Sciences*, 2010, **2**(4), 6610–6625.
50 A. C. Kaushik, S. Bharadwaj, S. Kumar and D. Q. Wei, Nanoparticle mediated inhibition of Parkinson's disease using computational biology approach, *Sci. Rep.*, 2018, **8**(1), 9169.
51 S. P. Singh and S. Urooj, Combined rotation-and scale-invariant texture analysis using radon-based polar complex exponential transform, *Arab. J. Sci. Eng.*, 2015, **40**, 2309–2322.
52 S. P. Singh and S. Urooj, Three Types of Moment Invariants for Color Object Recognition Based on Radon and Polar Harmonic Transform in Cℓ (0, 2) Space, *Arab. J. Sci. Eng.*, 2016, **41**, 3051–3060.
53 E. N. Wilson, *et al.*, NP03 inhibits BACE1 and GSK-3B for the prevention of earlyalzheimer's-like amyloid neuropathology in transgenic rats, *Alzheimer's and Dementia*, 2016, **12**(7), P834.
54 E. J. Adolph, A. E. Hafeman, J. M. Davidson and L. B. Nanney, Nanotechnology in bone tissue engineering, *Nanomedicine*, 2015, **11**, 1253–1263.
55 C. J. Thompson, *et al.*, Enzymatic synthesis and evaluation of new novel ω-pentadecalactone polymers for the production of biodegradable microspheres, *J. Microencapsul.*, 2006, **23**(2), 213–226.
56 B. V. Basavaraj, *et al.*, Hollow microspheres of diclofenac sodium - A gastroretentive controlled delivery system, *Pak. J. Pharm. Sci.*, 2008, **21**(4), 451–454.
57 N. R. Kadam, Microsphere: A Brief Review, *Asian J. Biomed. Pharm. Sci.*, 2015, **5**(47), 13–19.
58 I. D. Rosca, F. Watari and M. Uo, Microparticle formation and its mechanism in single and double emulsion solvent evaporation, *J. Controlled Release*, 2004, **99**(2), 271–280.
59 P. B. O'Donnell and J. W. McGinity, Preparation of microspheres by the solvent evaporation technique, *Adv. Drug Delivery Rev.*, 1997, **28**(1), 25–42.
60 S. Tiwari and P. Verma, Microencapsulation Technique by Solvent Evaporation Method (Study of Effect of Process Variables), *Int. J. Pharm. Life Sci.*, 2011, **2**(8), 998–1005.
61 C. C. Wang, A. L. Chen and I. H. Chen, Preparation of a highly luminescent nanocomposite by chelating copolymer, *Polym. Adv. Technol.*, 2006, **17**(7–8), 598–603.
62 J. Bux, M. S. Manga, T. N. Hunter and S. Biggs, Manufacture of poly(methyl methacrylate) microspheres using membrane emulsification, *Philos. Trans. R. Soc., A*, 2016, **374**(2072), 20150134.
63 A. C. Kaushik, *et al.*, Deciphering the Biochemical Pathway and Pharmacokinetic Study of Amyloid βeta-42 with Superparamagnetic Iron Oxide Nanoparticles (SPIONs) Using Systems Biology Approach, *Mol. Neurobiol.*, 2018, **55**(4), 3224–3236.
64 H. Kawaguchi, Functional polymer microspheres, *Prog. Polym. Sci.*, 2000, **25**(8), 1171–1210.
65 M. Jorfi and E. J. Foster, Recent advances in nanocellulose for biomedical applications, *J. Appl. Polym. Sci.*, 2015, **132**(14), DOI: 10.1002/app.41719.
66 Y. Wang, *et al.*, PubChem: A public information system for analyzing bioactivities of small molecules, *Nucleic Acids Res.*, 2009, **37**(suppl_2), W623–W633.
67 K. J. Bowers, *et al.*, Molecular dynamics—Scalable algorithms for molecular dynamics simulations on commodity clusters, *Proceedings of the 2006 ACM/IEEE conference on Supercomputing - SC '06*, 2006, vol. 11, p. 43.
68 W. Jiang, *et al.*, Generalized scalable multiple copy algorithms for molecular dynamics simulations in NAMD, *Comput. Phys. Commun.*, 2014, **185**(3), 908–916.
69 P. Hinderliter and S. A. Saghir, Pharmacokinetics, *Encyclopedia of Toxicology*, 3rd edn, 2014, pp. 762–764, DOI: 10.1016/B978-0-12-386454-3.00419-X.
70 Chemical engineering kinetics, *AIChE J.*, 1956, **2**, 281.
71 R. Friedman, Chemical equilibrium, *SFPE Handbook of Fire Protection Engineering*, 5th edn, 2016.

Published on 24 June 2019. Downloaded by National Sun Yat Sen University on 3/23/2020 10:57:07 AM.

72 A. B. García, A. Cuesta, M. A. Montes-Morán, A. Martínez-Alonso and J. M. D. Tascón, Zeta potential as a tool to characterize plasma oxidation of carbon fibers, *J. Colloid Interface Sci.*, 1997, **192**, 363–367.
73 R. Marsalek, Particle Size and Zeta Potential of ZnO, *APCBEE Proc.*, 2014, **9**, 13–17.
74 K. S. Suganthi and K. S. Rajan, Temperature induced changes in ZnO-water nanofluid: Zeta potential, size distribution and viscosity profiles, *Int. J. Heat Mass Transfer*, 2012, **55**, 7969–7980.
75 S. P. Singh and S. Urooj, An Improved CAD System for Breast Cancer Diagnosis Based on Generalized Pseudo-Zernike Moment and Ada-DEWNN Classifier, *J. Med. Syst.*, 2016, **40**, 105.
76 S. P. Singh, *et al.*, Breast cancer detection using PCPCET and ADEWNN: A geometric invariant approach to medical X-ray image sensors, *IEEE Sens. J.*, 2016, **16**, 4847–4855.
77 A. Funahashi, M. Morohashi, H. Kitano and N. Tanimura, CellDesigner: a process diagram editor for gene-regulatory and biochemical networks, *BIOSILICO*, 2003, **1**(5), 159–162.

 This journal is © The Royal Society of Chemistry and the Centre National de la Recherche Scientifique 2019